



Boosting and stabilizing oxygen evolution reaction through Ru single atoms anchored amorphous NiMoO_x electrocatalyst

Received: 11 March 2025

Accepted: 2 September 2025

Published online: 03 October 2025

Jiayi Li^{1,9}, Yiming Zhu^{1,9}, Changyuan Li^{1,2}, Qian Zhang³, Ju Rong⁴, Shasha Guo¹, Nicolas Alonso-Vante⁵, Long Yang^{1,2}, Min-Hsin Yeh^{1,6,7}, Wei-Hsiang Huang^{1,7,8}✉, Xiaohua Yu^{1,4}✉, Hongfei Cheng¹✉ & Jiwei Ma¹✉

Check for updates

Efficient and durable electrocatalysts for the oxygen evolution reaction (OER) are essential for advancing water splitting technologies, which enable sustainable hydrogen production. The integration of amorphous oxide supports with metal single atoms offers a promising strategy to precisely tuning the electronic structure and improving the exposure of active sites. Here, we report an amorphous NiMoO_x support anchored with Ru single atoms (denoted as a-RNMO), which achieves a low cell voltage of 1.78 V at 1 A cm⁻² and noteworthy durability in an anion exchange membrane water electrolyzer. Time-resolved operando Quick X-ray absorption spectroscopy reveals rapid Mo leaching followed by structural reconstruction, culminating in the NiOOH formation. Theoretical calculations suggest a likely “complementary amorphous-electronic” mechanism. It shows that the amorphous structure exposes more active sites and favors the adsorption of intermediates, while Ru single atoms finely modulate the electronic structure. These valuable insights highlight the design of high-performance OER electrocatalysts based on metal single atoms anchored on amorphous oxides.

The oxygen evolution reaction (OER) is a key reaction in water splitting for hydrogen production and metal-air batteries^{1,2}. Since this is a slow four-electron transfer reaction, highly efficient electrocatalysts are required to accelerate the process³. Although noble-metal catalysts such as Ru and Ir oxides show excellent intrinsic OER activity, their large-scale application is limited by high cost and scarcity^{4,5}. Therefore, the research interest has shifted towards non-noble 3d transition-metal (hydro)oxides. These non-noble metal catalysts are cost-effective and

can maintain competitive electrocatalytic performance^{6,7}. Among them, Ni complies the Sabatier principle for electrocatalyst design and has thus attracted significant research interest. In Ni-based materials (e.g., MOFs^{8,9}, NiMoO₄^{10,11}, LiNiO₂¹², Ni(OH)₂^{13,14}, and Ni-based LDHs¹⁵), electrocatalytic oxidation induces the surface reconstruction into hydroxides, which are widely considered to be the real active sites. Recently, amorphous oxides have also been shown to display promising electrocatalytic properties. Amorphous structures typically

¹Shanghai Key Laboratory for R&D and Application of Metallic Functional Materials, Institute of New Energy for Vehicles, School of Materials Science and Engineering, Tongji University, Shanghai, China. ²Interdisciplinary Materials Research Center, School of Materials Science and Engineering, Tongji University, Shanghai, China. ³Key Laboratory of Advanced Civil Engineering Materials of Ministry, School of Materials Science and Engineering, Tongji University, Shanghai, China. ⁴Faculty of Materials Science and Engineering, Kunming University of Science and Technology, Kunming, China. ⁵College of Smart Energy, Shanghai Jiao Tong University, Shanghai, China. ⁶Department of Chemical Engineering, National Taiwan University of Science and Technology, Taipei, Taiwan. ⁷Sustainable Electrochemical Energy Development (SEED) Center, National Taiwan University of Science and Technology, Taipei, Taiwan. ⁸National Synchrotron Radiation Research Center (NSRRC), Hsinchu, Taiwan. ⁹These authors contributed equally: Jiayi Li, Yiming Zhu. ✉e-mail: huang.sean@nsrrc.org.tw; xiaohua_y@163.com; cheng_hongfei@tongji.edu.cn; jiwei.ma@tongji.edu.cn

exhibit a larger electrochemical surface area and more abundant defects, which can facilitate adsorption and desorption of intermediates and also expose richer active sites¹⁶. NiMo-based amorphous oxides are attracting attention due to their facile synthesis (e.g., room-temperature preparation), fast surface reconstruction rate¹⁷, and experimental feasibility. However, significant efforts are still needed in electronic structure modulation to further enhance the OER performance of this type of electrocatalyst.

Meanwhile, numerous previous theoretical and experimental studies have shown that single atom catalysts (SACs), due to their minimal metal usage and specific coordination environments^{18–21}, can be promising candidates with tunable electronic structure and potentially improved electrocatalytic performance. However, several hurdles remain to be overcome before SACs can serve as a competent catalyst. One of the challenges is how to anchor or expose more single-atom metal sites to modulate their local microenvironment²². Amorphization creates an abundance of metal dangling bonds with flexible unsaturated electronic configurations, providing more opportunities for electronic coupling, redistributing local lone-pair electrons, and accelerating charge transfer between active centers^{15,23,24}. Inspired by these findings, it is speculated that incorporating single atoms into amorphous structures could be a viable approach to enhance their catalytic activities. On the other hand, the rapid reconstruction characteristics of amorphous materials place higher demands on detection techniques. It remains challenging to comprehensively identify surface transformations in Ni-based amorphous OER catalysts, and this area has received little attention. Conventional synchrotron beamlines based on monochromators require several minutes to acquire a complete X-ray absorption spectrum, which greatly limits the temporal resolution that can be achieved²⁵. In this regard, the rapid reconstruction of Ni-based amorphous oxides may be overlooked. Recent advances in the so-called quick-X-ray absorption fine structure (QXAFS) method, which employs fast data acquisition schemes and specially designed continuous-scanning monochromators, allow temporal resolutions down to the millisecond range²⁶. This allows us to investigate the details of the experimental design and probe the structural changes of Ni-based amorphous oxides.

Inspired by these results, we developed a room-temperature strategy to anchor Ru single atoms onto amorphous NiMoO_x (a-RNMO) via a one-step supersaturated co-precipitation method. The as-prepared a-RNMO, with low Ru single-atom loading (2.28 at.%), required only 1.78 V to reach 1 A cm^{-2} in an anion exchange membrane water electrolyzer (AEMWE) device, maintaining stability for over 100 hours. Comprehensive characterization revealed the dynamic reconstruction during oxidation, ultimately forming the amorphous NiOOH . Density functional theory (DFT) calculations suggest that Ru single atoms could contribute to tuning the amorphous electronic structure, and also indicate that electronic interaction between Ru and Ni could facilitate the adsorption of intermediate oxygen. This work presents the concept of anchoring metal single atoms in synthetic amorphous oxides and its potential influence on alkaline OER, and proposes a complementary amorphous-electronic mechanism.

Results

Synthesis and structural characterization of the amorphous materials

For materials synthesized at room temperature, it is crucial to find metals that can co-precipitate simultaneously in the system with sufficiently rapid precipitation kinetics; otherwise, phase separation may occur²⁷. A facile one-step supersaturated co-precipitation method was used to prepare a-RNMO. In brief, high-concentration aqueous solutions of Ni^{2+} , Ru^{3+} , and MoO_4^{2-} were prepared separately and then quickly mixed under ultrasonication, leading to the instantaneous formation of metal-oxide precipitates, according to the schematic diagram in Fig. 1a. The a-RNMO was obtained through subsequent

washing and drying. The X-ray diffraction (XRD) pattern (Fig. 1b) showed the absence of a crystalline phase in a-NMO and a-RNMO, which was distinct from crystalline NiMoO_4 (c-NMO) with strong characteristic peaks. The absence of diffraction peaks limits the information extractable from XRD analysis, emphasizing the need for high-energy synchrotron X-ray total scattering measurements with pair distribution function (PDF) analysis. This technique provides short-range structural correlations of amorphous structure by Fourier transform of the total scattering data (including both diffuse and Bragg)^{28,29}. As shown in Fig. 1c-e, it was evident that for the pristine a-NMO and a-RNMO, the crystal structures were long-range disordered but short-range ordered, in contrast to c-NMO which had a long-range ordered crystal structure. This analysis indicated that the amorphous structure had a short-range correlation of about 9 Å. The local structures of a-NMO and a-RNMO can be modeled using the crystal structure of NiMoO_4 (PDF#33-0948, Supplementary Fig. 1). Compared with the c-NMO results, the M–O (M = Ni, Mo) and M–M bond lengths in the amorphous structures were found to be longer. This suggested that the amorphous structure was looser, which could expose more active sites in the electrocatalytic reaction and potentially enhance the adsorption and desorption capacity of OER intermediates. In the a-RNMO structure, the average M–O bond length (1.90 Å) was slightly longer than that of a-NMO (1.86 Å), probably due to the larger atomic radius of Ru. Detailed results of the PDF structural refinements are provided in Supplementary Table 1. As shown in Supplementary Fig. 2a, a-RNMO exhibited uniform nanoparticle morphology with an average size of about 50 nm. The high-resolution transmission electron microscopy (HR-TEM) image in Supplementary Fig. 2b-c showed no lattice fringes, combined with the absence of diffraction rings in the selected area electron diffraction (SAED) pattern (Supplementary Fig. 2d), together indicating typical amorphous oxide formation. The a-NMO exhibited similar features (Supplementary Fig. 3). In contrast, c-NMO (Supplementary Fig. 4) consisted of short nanorods, and its HR-TEM images displayed clear lattice fringes, confirming a high degree of crystallinity. Supplementary Fig. 5 and Fig. 6 show the uniform distributions of Ni, Mo, and O elements in a-NMO and c-NMO, respectively. The presence of monodispersed Ru single atoms (bright dots marked by red circles in Fig. 1f) was observed by high-magnification aberration-corrected high-angle annular dark-field scanning transmission electron microscopy (AC-HAADF-STEM) image. Fig. 1g shows the 3D surface plot of the selected region in Fig. 1f. No obvious atomic lattice distribution was observed, and the intensity of atomic signals appeared random, which is characteristic of amorphous structures. The highest peaks corresponded to the positions of Ru single atoms, further demonstrating their isolated dispersion. Moreover, energy-dispersive X-ray spectroscopy (EDS) mapping (Fig. 1h) revealed homogeneous spatial distribution of Ru, Ni, Mo, and O. The elemental composition of a-RNMO was analyzed by inductively coupled plasma-optical emission spectroscopy (ICP-OES) (Supplementary Table 2) and scanning electron microscopy-energy-dispersive X-ray spectroscopy (SEM-EDS) (Supplementary Fig. 7), confirming the Ru content was 2.28 at.%. The molar ratio of Ru to Ni (≈ 0.15) was higher than the theoretical value, which could be attributed to higher loss of Mo and Ni ions compared to Ru ions during supersaturated solution processing. As a result, the amorphous structure accommodated more Ru single atoms in a homogeneous manner.

Electronic structure and oxidation state analysis

We investigated the influence of amorphous phase and Ru incorporation on the electronic structure and coordination environment of Ni and Mo by X-ray photoelectron spectroscopy (XPS) and X-ray absorption spectroscopy (XAS). As shown in Fig. 2a, the two main Ni 2p peaks of both a-NMO and a-RNMO were deconvoluted into Ni^{2+} (about 855 eV and 873 eV) and Ni^{3+} (about 857 eV and 875 eV) species, respectively¹⁰. The incorporation of Ru resulted in an increased

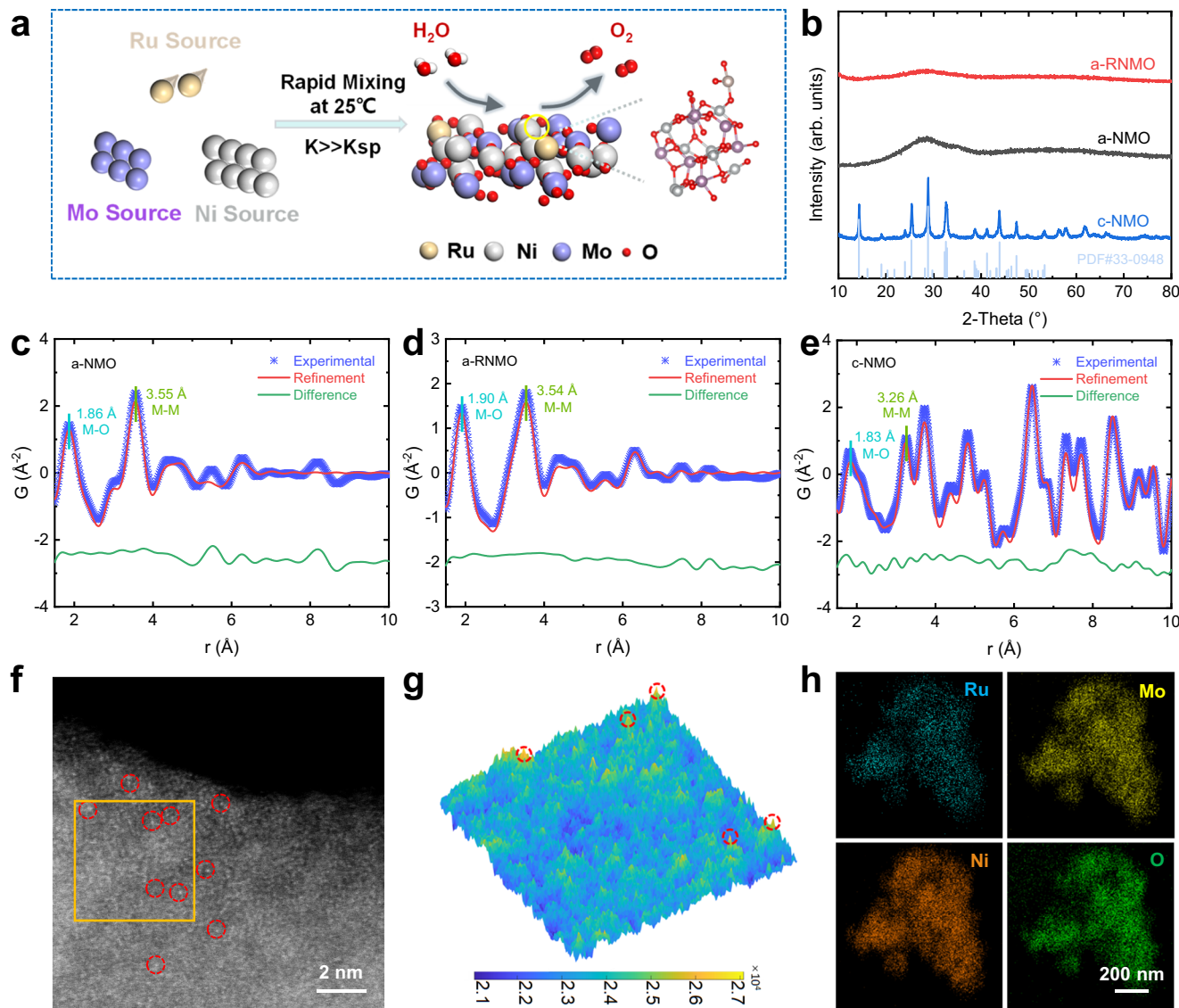


Fig. 1 | Structural characterizations of amorphous RuNiMo oxides (a-RNMO). **a** Schematic illustration of the amorphous catalyst synthesis via one-step co-precipitation method. The white, red, grey, purple, and yellow spheres represent H, O, Ni, Mo, and Ru, respectively. **b** XRD patterns of a-NMO, a-RNMO, c-NiMoO₄.

where the X-ray PDFs at room temperature (blue) are fitted by the NiMoO₄ structural model (red) over the range of $1.5 < r < 10 \text{ \AA}$. The difference curve (green) is shown offset below. **f** AC-HAADF-STEM image of a-RNMO. **g** 3D atom-overlapping surface plots of the selected area in **(f)**. **h** EDS mappings of a-RNMO. Source data for the Figure **(b–e, g)** are provided as a Source Data file.

proportion of Ni²⁺ and a peak shift towards lower binding energy. Specifically, the percentage of Ni²⁺ species increased from 69% in a-NMO to 78% in a-RNMO, suggesting that the surface average valence state of Ni was reduced in the presence of Ru. As for the Mo 3d spectra in Fig. 2b, the peaks corresponded to the Mo⁶⁺ signal^{30,31}. The shape and position of these peaks were similar for both a-NMO and a-RNMO, indicating that Mo⁶⁺ was unaffected by Ru. The valence state of Ru in a-RNMO, as shown in Fig. 2c, was approximately Ru^{3.60+}. The O 1s spectra of a-RNMO (Supplementary Fig. 8) showed a higher lattice oxygen concentration (M-O) than that of a-NMO³², suggesting that the introduction of Ru favored an increase ratio of the lattice oxygen.

XAS is a powerful tool for studying electronic and local structure properties. The X-ray absorption near edge structure (XANES) spectra at the K-edge correspond to transitions of the 1s core electrons to unoccupied orbitals^{33–35}, revealing the bulk chemical states of Ni, Mo, and Ru ions. The edge position is sensitive to the oxidation state³⁶. As observed in Fig. 2d, the normalized Ni K-edge XANES

spectra showed a slight decrease in the valence state of Ni species by the introduction of Ru, suggesting partial electron donation from Ru to Ni, leading to the slight Ni reduction. This electron transfer between Ru and Ni was consistent with XPS results. In contrast, the Mo K-edge spectra exhibited similar shapes and edge positions for a-NMO and a-RNMO (Fig. 2e), indicating a nearly identical valence state³⁷, which is close to Mo⁶⁺ (c-NiMoO₄). For the K-edge of Ru (Fig. 2f), the edge position in a-RNMO was negatively shifted compared to RuO₂, implying a slightly lower valence state than Ru⁴⁺. This was in agreement with XPS analysis. Extended X-ray absorption fine structure (EXAFS) spectra were further employed to study the coordination environment of a-RNMO. The R-space were obtained by Fourier transform (FT) of the measured k-space data, which exhibited a high signal-to-noise ratio up to 8 \AA^{-1} (Supplementary Fig. 9). FT analysis of a-RNMO and a-NMO revealed reduced structural order compared to c-NMO, as evidenced by the lower amplitudes of FT peaks of a-d³³ (Fig. 2g). The first coordination shell corresponded to Ni-O bonds ($\sim 1.59 \text{ \AA}$) in the amorphous structure, slightly longer than

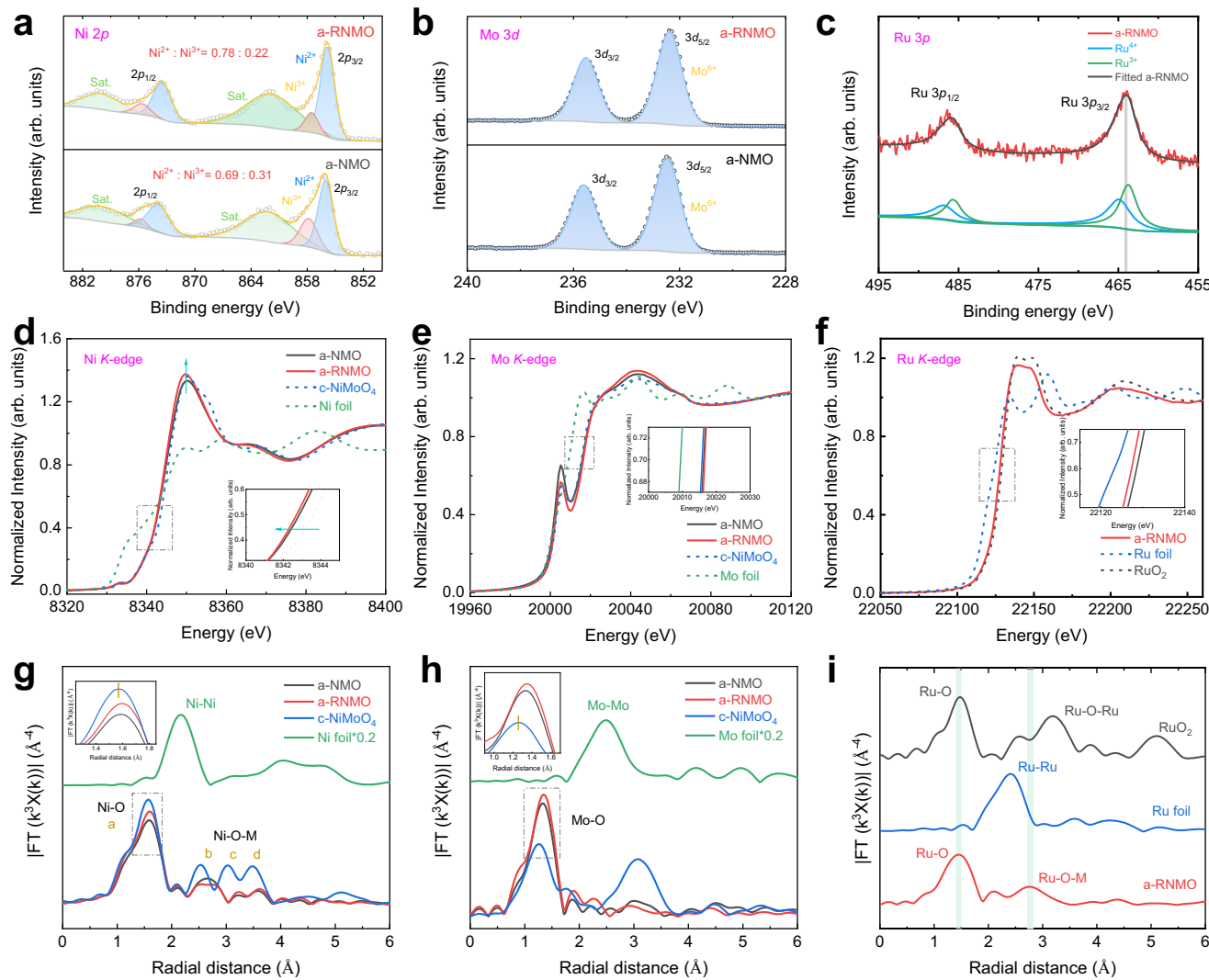


Fig. 2 | Surface XPS and bulk XANES, EXAFS analysis of a-RNMO. **a** Ni 2p and **(b)** Mo 3d XPS spectra of a-NMO and a-RNMO. **c** Ru 3p XPS spectrum of a-RNMO. **d** The normalized Ni K-edge and **(e)** the normalized Mo K-edge XANES spectra of a-NMO, a-RNMO, and c-NiMoO₄. **f** The normalized Ru K-edge XANES spectra of a-RNMO, Ru foil, and RuO₂. The magnitude of the Fourier transforms for **(g)** Ni K-edge, and **(h)** Mo K-edge EXAFS spectra of a-NMO, a-RNMO, and c-NiMoO₄. **i** Ru K-edge EXAFS spectra a-RNMO, Ru foil, and RuO₂. Source data for the Figure (a–i) are provided as a Source Data file.

those in the crystalline structure, which could facilitate higher exposure of active sites for electrocatalysis. A similar trend was observed for the Mo K-edge results (Fig. 2h). The Mo–O distances in a-NMO and a-RNMO were 1.32 Å and 1.35 Å, respectively, which were longer than that of c-NMO (~1.26 Å). No evident Ni–Ni and Mo–Mo scattering signals were detected, indicating an absence of metal clusters. The Ru K-edge EXAFS spectra (Fig. 2i) of a-RNMO showed two notable peaks in R-space. The main peak at ~1.44 Å corresponded to the Ru–O coordination shell. The second peak at ~2.76 Å differed from the Ru–Ru bond (~2.39 Å, from Ru foil) and Ru–O–Ru bond (~3.19 Å, from RuO₂), suggesting that the absence of Ru and RuO₂ nanoclusters in a-RNMO. The peaks at higher R might arise from higher frequency noise³⁸. In addition, there were two characteristic regions recognized by the wave transform (WT)-EXAFS analysis. As observed in Supplementary Fig. 10, the first and second shell scattering peaks were located at $R = 1.45 \text{ \AA}$, $k = 5.69 \text{ \AA}^{-1}$, and $R = 2.75 \text{ \AA}$, $k = 7.60 \text{ \AA}^{-1}$, respectively. This was quite different from the Ru–Ru and Ru–O–Ru bond positions, implying the presence of mono-dispersed Ru species. These structural characterizations, together with microscopy observations, demonstrated that Ru single atoms were homogeneously dispersed in a-RNMO.

Electrochemical alkaline OER performance investigation

The OER performance of amorphous electrocatalysts was evaluated in 1 M KOH using a three-electrode system. All measured potentials were carefully calibrated versus the reversible hydrogen electrode (RHE) (Supplementary Fig. 11). As shown in Fig. 3a, a-RNMO exhibited the highest OER activity among all investigated samples. At a current density of 10 mA cm⁻², the overpotential (η) of a-RNMO was 220 mV, substantially lower than those of a-NMO (326 mV) and c-NMO (450 mV). In addition, the overpotential of a-RNMO was lower than those of commercial RuO₂ and NiFe-LDH (Supplementary Fig. 12), the latter now being widely employed as a benchmark OER electrocatalyst. The polarization curves without iR compensation are provided in Supplementary Fig. 13. Moreover, the electrocatalytic OER performance of a-RNMO was optimized by adjusting the Ru content (Supplementary Fig. 14). These results suggested that an appropriate Ru concentration could enhance the OER performance of a-RNMO, possibly by tuning its overall electronic structure. Likewise, a-RNMO displayed the lowest Tafel slope (45.15 mV dec⁻¹), implying faster OER kinetics than others (Fig. 3b). Indeed, Tafel slopes were obtained from the linear relationship between overpotential and log(j) (Supplementary Fig. 15). As shown in Fig. 3c, electrochemical impedance

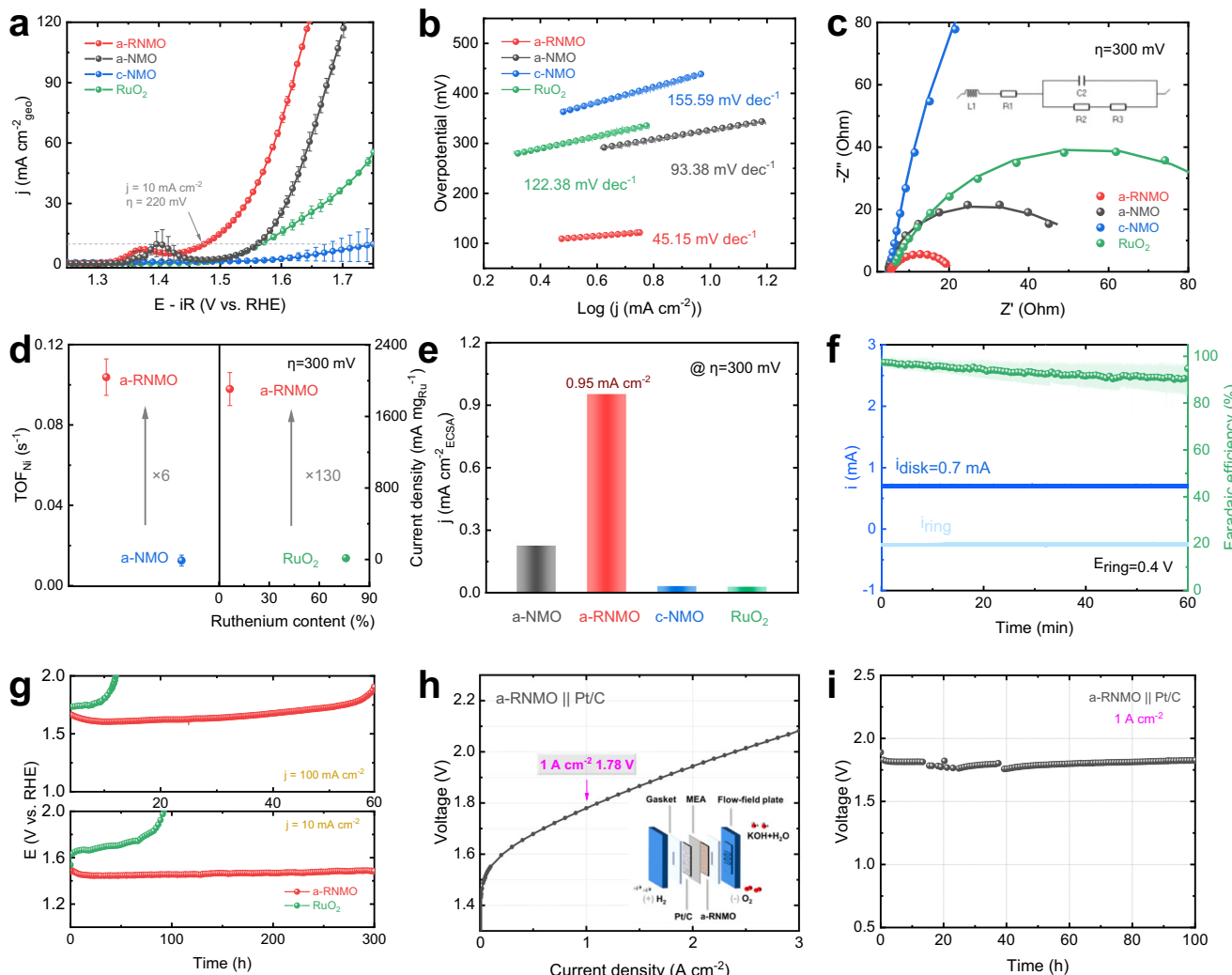


Fig. 3 | Electrochemical performance investigation of a-RNMO. **a**, LSV polarization curves with automatic iR-compensation of a-NMO, a-RNMO, c-NMO, and RuO₂ (mass loading: 0.255 mg cm⁻²) in 1 M KOH under 25 °C, at scan rate of 5 mV s⁻¹, using RDE (0.196 cm²) with 1600 rpm. **b**, Tafel plots extracted from (a). **c**, EIS Nyquist plots of samples at 1.53 V vs. RHE. (Inset: the equivalent circuit used) The charge transfer resistances (R_{ct}) of a-RNMO, a-NMO, c-NMO, and RuO₂ were $15.33 \pm 0.36 \Omega$, $48.82 \pm 0.76 \Omega$, $890.70 \pm 9.86 \Omega$, and $101.80 \pm 1.18 \Omega$, respectively. **d**, TOF values normalized to Ni and mass activities normalized to Ru at the overpotential of 300 mV. **e**, Specific activities of a-RNMO and others. **f**, FE tests of a-RNMO with RRDE

with 1600 rpm at $E_{ring} = 0.4$ V vs. RHE. **g**, Chronopotentiometry tests of a-RNMO and RuO₂ at 10 mA cm⁻² and 100 mA cm⁻², using carbon paper electrode (1 cm²). **h**, Polarization curve of the electrolyzer without iR-compensation using a-RNMO as the anode and Pt/C as the cathode in flowing 1 M KOH solution at 80 °C. (Inset: schematic illustration of AEMWE cell created by Microsoft PowerPoint) **i**, Durability of AEMWE at a current density of 1 A cm⁻² without iR-compensation at 80 °C. Note: The error bars represent the standard deviation of three independent measurements. Source data for the Figure (a–i) are provided as a Source Data file.

spectroscopy (EIS) Nyquist plots were measured under identical condition ($\eta = 300$ mV). Using the equivalent-circuit model (inset of Fig. 3c) for fitting, a-RNMO showed the smallest Nyquist semicircle and the lowest charge-transfer resistance (R_{ct}) (Supplementary Table 3), suggesting faster charge transfer during the OER process. To minimize the effect of morphology, the OER currents were normalized to the specific Brunauer–Emmett–Teller (BET) surface area (Supplementary Fig. 16). The specific activity of a-RNMO was more than 10 times higher than that of a-NMO. As shown in Fig. 3d, the turnover frequency (TOF) was calculated by assuming Ni as active site. Compared to a-NMO, the TOF of a-RNMO increased by approximately sixfold. The mass activity of a-RNMO (1906.87 mA mg⁻¹_{Ru}) was more than 140 times higher than that of RuO₂ (13.09 mA mg⁻¹_{Ru}). This combination of lower Ru content and higher mass activity indicates favorable utilization efficiency of Ru atoms in a-RNMO. Furthermore, to evaluate the true catalytic activity of electrocatalysts, the electrochemically active surface area (ECSA) was estimated from double-layer capacitance (C_{dl}) measurements

(Supplementary Fig. 17). The a-RNMO presented the highest specific activity (0.95 mA cm⁻²_{ECSA}), approximately fourfold than that of a-NMO (0.23 mA cm⁻²_{ECSA}) (Fig. 3e). The a-RNMO electrode also achieved a Faradaic efficiency (FE) over 90% during 60 minutes (Fig. 3f). A schematic diagram of the FE test is provided in Supplementary Fig. 18. The calculated oxygen yield based on FE results was nearly equivalent to the theoretical value (Supplementary Fig. 19), indicating high selectivity during the OER process. As summarized in Supplementary Fig. 20, Fig. 21, Table 4, and Table 5, a-RNMO outperformed most reported Ru- and NiMo-based oxide OER catalysts in both Tafel slope and overpotential. To evaluate stability, a chronopotentiometry test was conducted. As shown in Fig. 3g, the alkaline OER activity of a-RNMO showed a negligible change at current density of 10 mA cm⁻² and 100 mA cm⁻² after 300 h and 60 h, respectively, outperforming the stability of RuO₂. In summary, this amorphous oxide synthesized at room temperature with atomically dispersed Ru demonstrated excellent OER activity and stability under alkaline

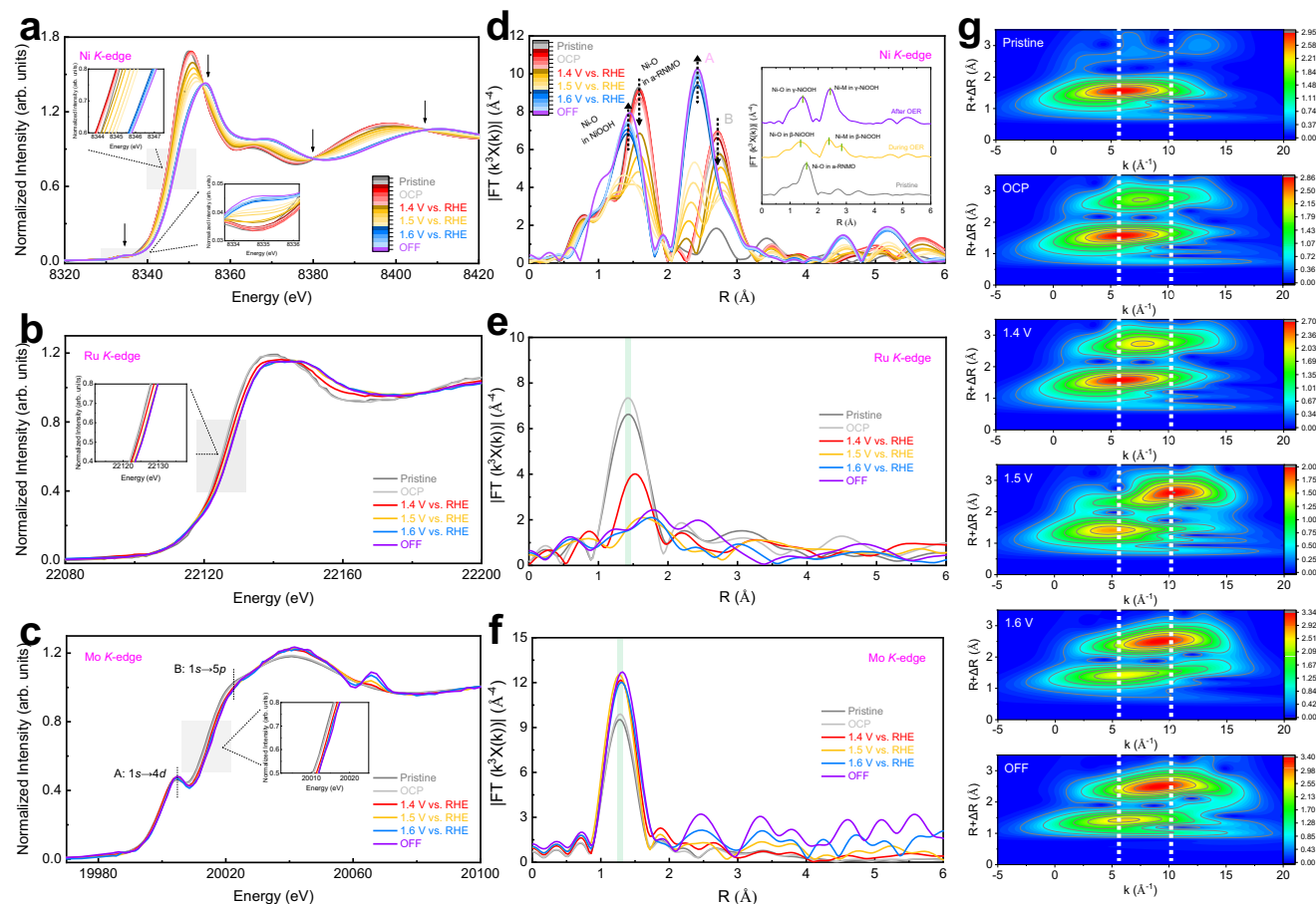


Fig. 4 | Operando XAS analysis of a-RNMO. **a–c** Ni K-edge, Ru K-edge, and Mo K-edge XANES spectra of a-RNMO measured in 1 M KOH under pristine, OCP, OER operating condition (1.4 V, 1.5 V, and 1.6 V vs. RHE) and OCP after OER operation. **d–f** The magnitude of the Fourier transforms for Ni K-edge, Ru K-edge, and Mo K-edge EXAFS spectra of a-RNMO measured in 1 M KOH under pristine, OCP, OER

operating condition (1.4 V, 1.5 V, and 1.6 V vs. RHE) and OCP after OER operation. **g** WT-EXAFS analysis of Ni K-edge under pristine, OCP, OER operating condition (1.4 V, 1.5 V, and 1.6 V vs. RHE) and OCP after OER operation. Source data for the Figure (a–g) are provided as a Source Data file.

conditions. Also, anion exchange membrane water electrolyzer (AEMWE) test further confirmed the promising performance of a-RNMO, achieving a cell voltage of 1.78 V at 1 A cm⁻² (Fig. 3h). Supplementary Fig. 22 compares the polarization behavior with commercial NiFe-LDH. The NiFe-LDH || Pt/C required 1.98 V at 1 A cm⁻², higher than that of a-RNMO. Moreover, no significant voltage increase was observed at 1 A cm⁻² over 100 h with a-RNMO (Fig. 3i). Polarization curves recorded during the durability test (Supplementary Fig. 23) confirmed that the catalytic activity was retained.

Mechanistic insights during the OER process

Exploring what changes in the OER process is of particular interest. To better understand the active site changes that might be responsible for the improved OER performance of a-RNMO, operando Quick-XAS data were collected sequentially at the Ni, Ru, and Mo K-edges to investigate the potential-dependent dynamics of oxidation states and coordination environments during the OER process. Unlike traditional operando measurements, the present study employed total-fluorescence-yield (TFY) mode Quick-XAS with a time resolution of about 2 min, revealing that the reaction which usually remained stable on a timescale of seconds to a few minutes. This is more suitable for observing dynamic variations of oxidation state under a constant potential over time, thus enabling a true operando measurement. The setup of the test is shown in Supplementary Fig. 24. During the measurements, XAS data were collected at open circuit potential (OCP), 1.4 V, 1.5 V, and 1.6 V versus RHE, respectively,

and finally returned to OCP, allowing time-dependent scanning every minute. As shown in Fig. 4a, the K-edge spectrum of Ni from pristine a-RNMO exhibited a pronounced edge and a high white-line signal around 8350 eV. As the potential increased and the reaction proceeded, the Ni K-edge continuously shifted toward higher energy by approximately 2 eV. In addition, the intensity of the white-line decreased, suggesting lower geometrical asymmetry with deeper oxidized Ni species. The results indicate that Ni species of a-RNMO underwent oxidation during the OER process, and the valence state of Ni appeared to increase gradually and irreversibly³⁹. In addition, the relative intensity of the pre-edge peak at 8334 eV was observed to rise with increasing potentials (inset of Fig. 4a), which was in response to a decrease in localized octahedral [NiO₆] symmetry⁸. Moreover, at least four discrete isosbestic points were identified in the K-edge XANES spectra of Ni in a certain range of oxidizing potential (black arrows in Fig. 4a), signifying that a continuous self-reconstruction process undergoes a linear combination of different Ni-based species^{8,40}. This trend was better demonstrated by the FT-EXAFS results obtained later. As shown in Fig. 4b, the K-edge of Ru underwent a slight positive shift when the applied voltage reached approximately 1.5 V, and its position remained nearly unchanged thereafter. Subsequently, operando Mo K-edge XANES (Fig. 4c) revealed a minor positive shift at OCP compared to pristine a-RNMO, possibly caused by partial electron delocalization due to the adsorbed H₂O. The pre-edge peak (labeled A) at 20004 eV was attributed to the dipole-allowed 1s→4d transition, indicating that all

compounds, under different voltages, Mo exhibited tetrahedral symmetry⁴¹⁻⁴³. The wide pre-edge shoulder (labeled B) at 2002 eV was associated with octahedrally coordinated Mo, corresponding to a $1s \rightarrow 5p$ transition⁴³. The Mo K-edge position varied slightly, implying that Mo was unlikely to serve as the main active site of a-RNMO during OER. FT-transformed EXAFS of K-edges of Ru, Ni, and Mo were characterized to investigate the coordination environments by time-dependent experiment.

FT-EXAFS of the Ni K-edge (Fig. 4d) showed that the first-shell Ni–O peak ($\sim 1.59 \text{ \AA}$) weakened below 1.4 V (red curves). Above 1.5 V (yellow and blue curves), a new peak at $\sim 1.40 \text{ \AA}$ emerged, corresponding to the Ni–O bond in β -NiOOH species. The higher the applied voltage, the more intense the signal was. After switching off potential (purple curves), two peaks at $\sim 1.45 \text{ \AA}$ and $\sim 1.05 \text{ \AA}$ were observed, attributed to the Ni–O bond in the γ -NiOOH species. The Ni–M peak ($\sim 2.73 \text{ \AA}$, labeled B) split into two peaks at 1.5 V, assigned to β -NiOOH. At 1.6 V, the peak at 2.42 \AA (labeled A) corresponded to γ -NiOOH^{13,44}. The inset in Fig. 4d provides a clear visualization of the species change process. WT-EXAFS (Fig. 4g) confirmed the emergence of a new Ni–M coordination at 1.5 V ($R = 2.61 \text{ \AA}$, $k = 10.45 \text{ \AA}^{-1}$). At 1.6 V, another Ni–M coordination ($R = 2.50 \text{ \AA}$, $k = 9.16 \text{ \AA}^{-1}$) was formed without showing reversibility after switching off potential. The interatomic distances were reduced through a denser form of edge-sharing polyhedral stacking in the oxidized state, resulting in the formation of NiOOH analogues^{8,45}. These observations suggest a two-step reconstruction of Ni species, undergoing first β -NiOOH and then γ -NiOOH. In the Ru K-edge EXAFS (Fig. 4e), the Ru–O bond signal at 1.45 \AA decreased with increasing potential, implying a lower coordination number. Ex-situ ICP-MS test was supplemented. As shown in Supplementary Fig. 25 and Table 6, the dissolution of Ru and Ni was negligible within 100 hours (below 0.25 ppm), while Mo loss was more than ten times to those of Ru and Ni. In the time-resolved operando XAS test, it only took two minutes to collect each spectrum. Therefore, the change in the Ru coordination environment cannot be related to the Ru dissolution, which is originated from the generation of unsaturated Ru active sites. The FT-EXAFS spectrum of Mo K-edge (Fig. 4f) showed a first shell signal at 1.30 \AA , corresponding to the Mo–O bond in a-RNMO. Its bond length remained almost constant during the OER process, further supporting that Mo was not the main active site.

In-situ Raman spectroscopy (Supplementary Fig. 26 and 27) was used to detect the intermediate states of the catalyst. The c-NMO maintained its Mo–O vibration modes (a very strong band at 959 cm^{-1} was the terminal Mo = O bond symmetric stretch, a band at 914 cm^{-1} was the terminal Mo = O bond asymmetric stretch, and a band at 704 cm^{-1} was the Ni–O–Mo bond symmetric stretch⁴⁶) up to 1.50 V without new species. The spectrum matched that of stoichiometric α -NiMoO₄⁴⁷. In contrast, a-RNMO and a-NMO showed different Raman shifts. The Mo–O feature at near 900 cm^{-1} , disappeared in a-RNMO above 1.30 V, suggesting a rapid Mo dissolution. The Mo–O signal of a-NMO persisted to 1.50 V, indicating a slower dissolution of Mo. Moreover, when the applied potential was above 1.25 V, a-RNMO displayed peaks at 470 cm^{-1} and 555 cm^{-1} , attributing to the bending vibrational mode of $E_g(\delta(\text{Ni}^{3+}-\text{O}))$ and the stretching vibrational mode of $A_{1g}(v(\text{Ni}^{3+}-\text{O}))$ in NiOOH. And, a-NMO showed similar characteristic peaks when the applied potential was above 1.35 V. Meanwhile, SEM and TEM (Supplementary Fig. 28) confirmed the retention of nanoparticles morphology and amorphous structure after OER. XRD (Supplementary Fig. 29) showed no new peaks appeared during 200 h stability test. SEM-EDS (Supplementary Fig. 30) revealed a substantial dissolution of Mo and a small amount of Ru loss. This behavior is common for alkaline electrocatalytic reactions with Mo element^{10,48-50}. XPS (Supplementary Fig. 31) further showed increased Ni valence and disappearance of Mo 3d peaks, testifying the dissolution of Mo. The elevated noise in k -space (Supplementary Fig. 32) also

supported the gradual Mo dissolution, which could facilitate the structural reconstruction in a-RNMO.

Theoretical considerations

To further elucidate the roles of the amorphous structure and Ru single atoms during the OER process, a theoretical study with DFT calculations was conducted. As for the amorphous atomic model, we thoroughly analyzed previous structural models and found their construction and validation to be scarce and challenging. In view of this, considering the compositional features by SEM-EDS spectra (Supplementary Fig. 7a), we selected NiMoO₄ with experimentally verifiable crystallographic characteristics (PDF#33-0948) as the benchmark model (Supplementary Fig. 33)⁵¹⁻⁵³. Through heating and cooling simulation tests at a rate of $20 \text{ }^{\circ}\text{C min}^{-1}$ to approximate the realistic amorphous state, the nearest neighbor coordination numbers were adjusted to match the experimental PDF analysis (Fig. 1c–e). The first coordination distances for c-NMO, a-NMO, and a-RNMO were computed as 1.75 \AA , 1.85 \AA , and 1.88 \AA , respectively (Supplementary Fig. 34), with an error margin of less than 0.1 \AA . In the a-RNMO model, Ru single atoms were introduced by replacing Ni atom on the surface according to the real Ni/Ru ratio. The calculated first coordination distance (1.88 \AA) deviated by less than 0.02 \AA from the experimental value, supporting the rationality of the model. Considering Mo dissolution during the structural evolution of a-RNMO over the OER process, an atomic model without Mo (a-Ru/NiOOH) was constructed. The POSCAR details of four structures, crystal NiMoO₄ (c-NMO), amorphous NiMoO_x (a-NMO), amorphous RuNiMoO_x (a-RNMO), and reconstructed NiOOH (a-Ru/NiOOH), can be seen in Supplementary Fig. 35.

We then compared the free energies of these different structures from three aspects: amorphous structures, single-atom effects, and reconstructed model. Regarding the amorphous structure, a comparison between c-NMO and a-NMO (Supplementary Fig. 36 and Fig. 5a) suggested that Ni sites act as the dominant active sites, and the *O adsorption step likely acts as the rate-determining step (RDS). The calculated theoretical overpotential of a-NMO (0.58 V) was lower than that of c-NMO (0.77 V, Supplementary Figs. 37, 38), which is in agreement with experimental observations. This reduction of the overpotential was attributed to the electronic modulation effect induced by the amorphous structure^{50,54}. The introduction of Ru single atoms in the model was found to lower calculated energy barriers (Fig. 5b), yielding an estimated overpotential of 0.51 V for a-RNMO compared with 0.58 V for a-NMO. The incorporation of Ru in a-RNMO reduced the free energies of formation of *OH and *O intermediates to 0.32 eV and 1.23 eV, respectively. It suggested that this modification could improve the reaction kinetics through electronic optimization (electronic interactions were discussed in detail in the next section). As shown in Fig. 5c and Supplementary Fig. 39, in single-site hypothetical cases, the overpotentials of Ni and Ru were calculated to be 0.61 V and 0.53 V, which are lower than NiOOH in the conventional adsorbate evolution mechanism (AEM, $\eta_{\text{NiOOH}} = 0.80 \text{ V}$) and lattice oxygen mechanism (LOM, $\eta_{\text{NiOOH}} = 0.88 \text{ V}$)⁵⁵. As shown in Supplementary Fig. 40, migration of *O between Ni and Ru (0.31 eV barrier at 300 K) suggested a possible dual-site cooperation in the model framework. Further understanding of the electronic mechanism underlying this synergistic dual-site effect required deeper investigation at the electronic structure level.

The complementary amorphous-electronic mechanism was systematically revealed at electronic-level, including charge density difference (CDD, Figs. 5d–g), projected density of states (PDOS, Supplementary Fig. 41), and molecular orbital theory (Fig. 5h). CDD in the simulated system indicated a notable charge redistribution after *O adsorption. Bader charge analysis suggested variations in electron transfer at the Ni sites from -1.09 e^- (a-RNMO) to -1.02 e^- (a-Ru/NiOOH). Concurrently, the Ru–Ni bond exhibited a delocalized charge

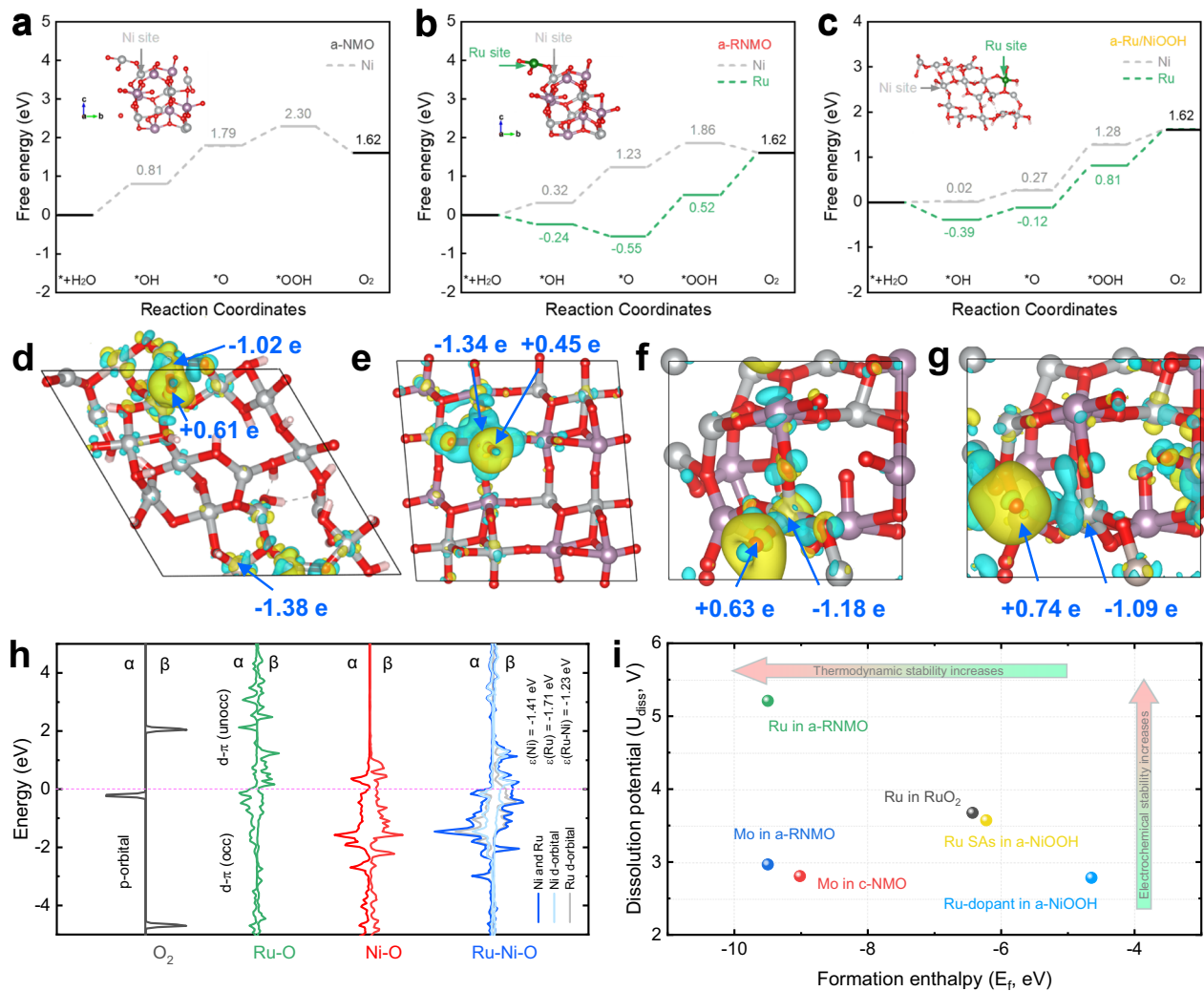


Fig. 5 | DFT calculations and OER mechanism of c-NMO, a-NMO, and a-RNMO. **a–c** Gibbs free energy diagram of the OER process on (a) a-NMO, (b) a-RNMO, and (c) a-Ru/NiOOH ($U=0$ V). The white, red, grey, purple, and green spheres represent H, O, Ni, Mo, and Ru, respectively. **d–g** CDD plots of oxygen adsorption in the RDS of (d) a-Ru/NiOOH, (e) c-NMO, (f) a-NMO, and (g) a-RNMO. (Electron accumulation is in yellow and depletion in blue, respectively. The blue-color numbers show the differences in electron transfer according to Bader's charge computations). **h** pDOS of *p* orbitals of O₂ gas molecule (left), *d* orbitals of Ni, Ru, Ni-Ru atoms (right), and *d* orbitals of their interaction within Ni-O and Ru-O (middle). **i** Computed formation enthalpy and dissolution potential of a-RNMO (including Mo and Ru ions), c-NMO (Mo ions), RuO₂ (Ru ions), a-Ru/NiOOH (Ru ions), and Ru-dopant in a-NiOOH (Ru ions). Source data for the Figure (a–c, h, i) are provided as a Source Data file.

differences in electron transfer according to Bader's charge computations). **h** pDOS of *p* orbitals of O₂ gas molecule (left), *d* orbitals of Ni, Ru, Ni-Ru atoms (right), and *d* orbitals of their interaction within Ni-O and Ru-O (middle). **i** Computed formation enthalpy and dissolution potential of a-RNMO (including Mo and Ru ions), c-NMO (Mo ions), RuO₂ (Ru ions), a-Ru/NiOOH (Ru ions), and Ru-dopant in a-NiOOH (Ru ions). Source data for the Figure (a–c, h, i) are provided as a Source Data file.

distribution characteristic. PDOS results showed an increase in electron occupied states near the Fermi level (E_f) and a shift of Ni *d*-band center to -1.41 eV, which could contribute to weaker *O adsorption. PDOS diagrams of other relevant catalysts are presented in Supplementary Fig. 42. Molecular orbital theory (Fig. 5h) implied potential Ru–Ni orbital interactions, while Ru might act as a bidirectional charge buffer. During O₂ generation, Ru functioned as an electron acceptor when Ni provided excess electrons ($\epsilon_{Ni} = -1.41$ eV), whereas during *OH desorption, Ru actively supplied electrons through the cooperative site ($\epsilon_{Ru-Ni} = -1.23$ eV) when Ni experienced electron deficiency. This dynamic response characteristic is clearly demonstrated in Supplementary Videos 1 and 2, which differs from previously reported unidirectional electron-donation systems, such as Fe-doped NiOOH⁵⁰, NiFeOOH⁴⁸, Zn/NiOOH⁵⁵, NiFeOOH@SO₄⁵⁶, and Ni(OH)₂/NiOOH⁵⁷. The operating mode resembled a seesaw mechanism, regulating both electronic site density and catalytic activity.

For the stability, the crystal orbital Hamilton population (COHP, Supplementary Fig. 43) quantitatively characterized the strength of atomic bonding, which is recognized as a well-established method for evaluating structural stability. The simulated bonding strength of

Ru–O (-5.46) was significantly higher than that in RuO₂ (-4.05), stabilizing Ru in a-RNMO. In contrast, the bonding strength of Mo–O in a-RNMO (-3.68) was weaker than that in c-NMO (-4.89), which would be responsible for severe Mo leaching under alkaline conditions. The COHP reflected the localized bond strength and exhibited an intrinsic correlation with the overall stability characterized by the formation enthalpy (E_f) the dissolution potential (U_{diss}), with reference to the definitions in the previous model⁵⁸. These two parameters collectively constituted the criteria for stability evaluation. Indeed, $E_f < 0$ eV and $U_{diss} > 0$ V versus standard hydrogen electrode (SHE) indicated thermodynamic stability and electrochemical stability, respectively. As shown in Fig. 5i and Supplementary Table 7, Ru in a-RNMO ($U_{diss} = 5.21$ V) was more stable than in RuO₂ ($U_{diss} = 3.67$ V), whereas Mo in a-RNMO exhibited a lower U_{diss} , suggesting the severe Mo dissolution, which are in agreement with experimental observations during OER. For the reconstructed NiOOH-related structures, two Ru configurations were compared (Supplementary Fig. 44): Ru single atoms anchored on the NiOOH surface and Ru doped into the NiOOH bulk. The calculated U_{diss} values (Fig. 5i) suggested that surface-anchored Ru single atoms were more stable than bulk-doped Ru. The corresponding

E_f values also indicated that atomically dispersed Ru on NiOOH was thermodynamically more favorable.

Discussion

In summary, amorphous NiMoO_x anchored with Ru single atoms was synthesized via a one-step supersaturated co-precipitation method at room temperature, improving OER activity and stability. Comprehensive physicochemical and operando characterizations, as well as DFT calculations, suggested that Ru single atoms and amorphous structure played vital roles in the electrocatalytic reactions. Notably, a-RNMO with 2.28 at.% Ru (220 mV overpotential) outperformed the commercial RuO₂ in mass and specific activities, offering significant economic advantages. Real-time operando XAS and in-situ Raman identified a continuous reconstruction during the OER process, culminating in the formation of crystalline and amorphous a-Ru/NiOOH. Unlike the conventional four-electron pathway, it was revealed that the amorphous structure with complementary electronic modulation that could facilitate OER performance. Moreover, a-RNMO demonstrated excellent performance in AEMWE, validating its potential for practical application in alkaline electrolyzer. This study provides a prospective strategy for anchoring noble metal single atoms in amorphous materials in order to strike a balance between high performance and economic efficiency. It also emphasizes the importance of conducting detailed spectroscopy measurements under operating conditions to understand the reconstruction during the evolution of Ni-based species.

Methods

Materials

Nickel(II) chloride hexahydrate (NiCl₂·6H₂O, 99.9%), sodium molybdate (Na₂MoO₄, ≥98%), ruthenium(III) chloride (RuCl₃, 99.5%), nickel(II) nitrate hexahydrate (Ni(NO₃)₂·6H₂O, 99.9%), and ammonium heptamolybdate tetrahydrate ((NH₄)₆Mo₇O₂₄·4H₂O, ≥99.9%) were purchased from Aladdin. Potassium hydroxide (KOH, 99.99%) was purchased from Sinopharm Chemical Reagent Co. Ltd (Shanghai, China). Ruthenium oxide (RuO₂, 99%) was obtained from Innochem.

Catalyst synthesis

Synthesis of amorphous NiMo oxides (a-NMO) and RuNiMo oxides (a-RNMO). The preparation of amorphous NiMo oxides and RuNiMo oxides was synthesized via the one-step supersaturated co-precipitation method. In a typical synthesis process, 20 ml of aqueous NiCl₂·6H₂O solution with a concentration of 1 M was prepared, denoted as solution A. 20 ml of aqueous Na₂MoO₄ solution with a concentration of 1 M and containing RuCl₃ was also prepared, denoted as solution B. The mass fraction of RuCl₃ in solution B were 1 at.%, 2.5 at.%, and 5 at.%. Then, solution B was rapidly added to solution A under ultrasonic conditions at room temperature. Precipitates were formed immediately. After 10 min of ultrasonic vibration, the precipitates were collected by centrifugation and washed with water and ethanol three times.

Synthesis of crystal NiMo oxides (c-NMO). 0.349 g Ni(NO₃)₂·6H₂O and 0.371 g (NH₄)₆Mo₇O₂₄·4H₂O were dissolved in 30 ml DI water and mixed under stirring for 30 min. Next, ammonium hydroxide was used to adjust pH = 7.0. The mixture was transferred into a Teflon-lined stainless-steel autoclave for hydrothermal treatment at 150 °C for 6 h. The precipitate was separated by centrifugation, washed with water and ethanol, and dried at 70 °C. The above products were annealed in air at 450 °C for 3 h, and the c-NMO was obtained.

Physical characterizations

General measurements. The samples were analyzed using XRD (Cu-K α source, λ_1 = 1.5405 Å, λ_2 = 1.5443 Å) on a Bruker D8 Advance diffractometer at 25 °C to identify phase purity and structural details.

XRD patterns were recorded in the 2θ range from 10° to 90°, and the scanning step was 0.02°. XPS (Thermo Scientific ESCALAB 250Xi, the US) was employed to characterize the electronic structure.

The morphology of samples was observed using SEM (Zeiss Sigma 500, Germany) at an accelerating voltage of 5 kV. The contents of the different elements were obtained by spot scanning in this model. TEM (JEOL 2100 F, Japan) and SAED were measured at a working voltage of 200 kV. EDS mapping was obtained in the HR-TEM model.

N₂ adsorption/desorption measurements were conducted using a TriStar 3020 device (Micromeritics Company, the US) using the Brunauer-Emmett-Teller (BET) analysis method. Metal ratios were measured using an ICP-OES (Agilent 730, the US). The lower concentration ratios of dissolution metal in electrolyte were measured by ICP-MS (Thermo Scientific iCAP RQ, the US).

A HORIBA XploRA PLUS Raman spectrometer, coupled with an electrochemical cell, was used to acquire operando Raman spectra. The working electrode was prepared by dropping pristine catalysts on carbon paper with 0.5 mg cm⁻² loading. Hg/HgO electrode and carbon rod were used as the reference electrode and counter electrode, respectively. Raman spectra were collected from 300 to 1000 cm⁻¹ while performing chronoamperometry test from 1.20 to 1.50 V vs. RHE in 1 M KOH solution to evaluate the reconstruction of catalysts.

X-ray PDF analysis and refinement. The synchrotron X-ray PDF measurements were carried out at the BL08W beamline at Super Photon ring-8 (Spring-8) in Japan using the rapid acquisition PDF method (RAPDF)^{59,60,61}. The incident beam energy was set to 114.11 keV, and the sample-to-detector distance was adjusted to 600.8797 mm. Powdered a-NMO, a-RNMO, and c-NMO samples were measured in 1-mm-diameter polyamide capillaries at room temperature. The detector exposure time was set to 240 s to ensure adequate counting statistics. The PDF data were processed and modeled with the software packages pyFAI, PDFgetX3, and PDFgui⁶²⁻⁶⁴. The Fourier-transform data were limited to Q ranges of 0.1–12.0 Å⁻¹ for both a-NMO and a-RNMO, and 0.1–17.0 Å⁻¹ for c-NMO. The instrument parameters for PDF modeling^{64,65} were obtained from a standard Silicon material and were determined to be $Q_{\text{damp}} = 0.02914 \text{ Å}^{-1}$ and $Q_{\text{broad}} = 0.0 \text{ Å}^{-1}$.

Quick-XAS measurement and analysis. Time-resolved operando quick-scanning XAS for this electrocatalysts were conducted in quick transmission mode at the TPS44A beamline in National Synchrotron Radiation Research Center (NSRRC) in Taiwan. Operando Quick-XAS data were sequentially carried out on the Ni, Mo and Ru K-edge to investigate the dynamics of oxidation states and coordination environments during the reaction process. We used a Quick-XAS in real time in 2 min to determine that the reaction was typically stable on a timescale of seconds or a few minutes, where a metal foil was taken as a reference to calibrate the energy scale. This was more conducive to observe the dynamic change of oxidation state with time under the same potential, which was also a true operando measurement. During the measurements, after collecting XAS data at the open circuit potential (OCP), the applied electrode potential was stepwise increased to 1.4 V, 1.5 V, and 1.6 V versus RHE, and then returned back to the OCP. Five spectra were collected at each potential, and each spectrum took only two minutes. For wavelet-transformed k^3 -weighted EXAFS, the $\chi(k)$ was exported from Athena.

Electrochemical measurements

Three-electrode cell measurements. All the OER measurements were tested in O₂-saturated 1 M KOH solution at room temperature on an electrochemical workstation (VMP3, Bio-Logic, France) with a rotating disk electrode (RDE) configuration. The electrolyte was prepared by dissolving 11.22 g of KOH pellets in 200 ml of DI water via stirring at room temperature for 10 minutes (pH = 13.7 ± 0.2). The electrolyte was freshly prepared for each measurement. A three-electrode

electrochemical cell was used for testing, including a glassy carbon (GC) electrode (0.196 cm²) as the working electrode, graphite electrode as the counter electrode, and Hg|HgO electrode as the reference electrode. The GC electrode was mechanically polished using Al₂O₃ powder to obtain a mirror-bright surface before measurements. The electrocatalysts (5 mg), Vulcan XC-72R (5 mg), and Nafion® solution (5.0 wt% in aliphatic alcohols, Aldrich) were dispersed in absolute isopropanol (1.9 ml) after 30 min of ultrasonic cell crusher. The 20 μl catalyst ink was then dropped onto the GC electrode and dried at the room temperature. The mass loadings of all electrocatalysts were about 0.255 mg cm⁻², including a-RNMO, a-NMO, c-NMO, and RuO₂. The noble metal Ru loading of a-RNMO and RuO₂ were 0.02 mg cm⁻² and 0.19 mg cm⁻², respectively. Linear sweep voltammetry (LSV) polarization curves were measured at 5 mV s⁻¹ in 0.0 ~ 1.0 V (vs. Hg|HgO) using RDE at 1600 rpm. Before LSV, cyclic voltammetry (CV) was measured at 50 mV s⁻¹ in 0.0 ~ 0.3 V (vs. Hg|HgO). A 95% iR compensation was automatically applied by the electrochemical workstation to minimize resonance effect and reduce significant data errors. Tafel plots were derived from the corresponding LSV polarization curves. The electrochemical impedance spectroscopy (EIS) was measured in the frequency range 0.01 ~ 100 kHz with an amplitude of 10 mV applied to the 1.53 V vs. RHE, averaging 6 data points per frequency decade. All data were fitted using ZView software to extract the relevant parameters. The turnover frequency (TOF) is calculated from

$$TOF = \frac{i}{4nF} \quad (1)$$

Here, i was obtained at overpotential 300 mV, n was the mole number of Nickel atoms on the electrode, and F was the Faraday constant. Based on the scan rate dependent of CV, during -0.1 V ~ 0.1 V (vs. Hg|HgO), at 100, 80, 60, 40, 20 mV s⁻¹, the double-layer charge (C_{dl}) was used to estimate the electrochemical surface area (ECSA). The ECSA is obtained from

$$ECSA = \frac{C_{dl}}{C_s} * S \quad (2)$$

Here, C_s was the specific capacitance of the corresponding smooth surface under the same conditions. In general, metal oxides had a value of C_s of 60 μF cm⁻². S is a surface area of working electrode (0.196 cm²). In addition, the Faradaic efficiency (FE) is obtained from rotating ring-disk electrode (RRDE) and calculated based on Eq. (3):

$$FE = \frac{I_{ring}}{C_e * I_{disk}} \quad (3)$$

Here, the collection current of I_{ring} was obtained at $E_{ring} = 0.4$ V vs. RHE and $I_{disk} = 0.7$ mA on the Pt electrode. The C_e is the oxygen collection coefficient which in this type of electrode configuration has a value of 0.37. To exclude interference of O₂ in the electrolyte, N₂ was passed throughout the FE test. It was ensured that all the O₂ generated by the OER occurring on the disk was utilized by the O₂ needed for the ORR occurring in the ring. The chronopotentiometry test was evaluated using carbon paper (1 cm², 0.255 mg cm⁻²) under different current density. Specifically, the catalyst ink was gradually drop-casted onto the carbon paper and dried at room temperature. The loading amount was determined by measuring the mass of the carbon paper before and after drop-casting. In H₂-saturated 1 M KOH, the calibration employed a Pt sheet working electrode, a Hg|HgO reference electrode, and a graphite rod counter electrode. CV scanning was carried out with 2 mV s⁻¹. The average potential value at the moment when the current becomes zero is the calibration value. In this study, all potentials were referenced to RHE.

AEMWE single-cell measurements. The membrane electrode assembly (MEA) fabrication and AEMWE evaluation were performed at Xiamen Kah Membrane Technology Ltd. The MEA was prepared by spraying technique of catalyst-coated substrate (CCS). For the anode, the prepared catalyst (a-RNMO) was dispersed in isopropanol and DI water, mixing with the ionomer solution. The prepared solution was manually sprayed on Ni foam as an anode gas diffusion electrode (GDE) with loading of 2 mg cm⁻². For the cathode, commercial Pt/C mixed was mixed in the same way. It was sprayed on carbon paper as a cathode GDE with loading of 1 mg cm⁻². The middle of the two electrodes was isolated by an anion exchange membrane (AEMO2-80 μm, Kah Membrane Technology). The membrane (thickness: 80 μm) was activated by soaking in 1 M KOH solution for 4 h at room temperature. The setup consisted of the prepared MEA, in addition to oxygen and hydrogen sides were equipped with PTFE gaskets, end plates with electrolyte ports, and bipotential plates. The CCSs were treated in 1 M KOH over 12 h before polarization test to access the activity. The components were clamped in a fixture with a torque of 3.5 N·m. The single-cell tests were carried out in flowing 1 M KOH solution at 80 °C, using chronoamperometry with stepwise increase in current, recording the change in voltage.

Computational methods

DFT calculations. DFT calculations in the first-principles framework were conducted with the Vienna Ab initio Simulation Package (VASP)^{66,67}. Throughout the calculations, the projector augmented wave (PAW) method and the Perdew-Burke-Ernzerhof (PBE) functional using the generalized gradient approximation (GGA) were applied^{68–71}. Convergence analysis determined energy cutoff of 500 eV in the plane-wave basis. Brillouin zone sampling was performed with a 3 × 3 × 1 k-point mesh using Monkhorst-Pack scheme⁷². To suppress spurious mirror-image interactions between adjacent unit cells, a 15 Å vacuum layer was incorporated perpendicular to the surface in slab-model simulations. The convergence criteria were established as 10⁻⁶ eV for electronic energy and 10⁻² eV/Å for atomic forces⁷³. Moreover, long-range dispersion interactions were corrected via the DFT-D3 method⁷⁴. The solvent effect of water has been treated implicitly using the VASPsol program⁷⁵. In addition, the charge transfer between the substrate and adsorbates was quantitatively described by means of Bader's charge analysis^{76,77}.

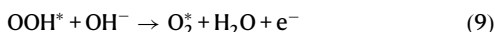
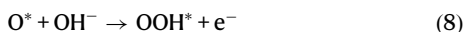
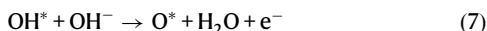
Formation enthalpy (E_f) and dissolution potential (U_{diss}). In addition to the intrinsic activity of the electrocatalysts, stability is also crucial. Some active sites may have good intrinsic activity, but there are many reasons why the actual activity is much lower than the theoretical intrinsic activity. For example, the central metal ion is easily dissolved, or the loading is susceptible to oxidation/reduction due to electron enrichment/deficiency. Taking the a-RNMO structure with the best performance as an example, its thermodynamic and electrochemical stabilities were evaluated by the formation enthalpy (E_f) and dissolution potential (U_{diss})⁵⁸, which were defined as

$$E_f = \frac{1}{2}(E_{a-RNMO} - E_{a-NMO} - E_{Ru}) \quad (4)$$

$$U_{diss} = U_{diss(Ru, a-RNMO)} - \frac{E_f}{ne} \quad (5)$$

where E_{a-RNMO} and E_{a-NMO} are the total energies of a-RNMO (with Ru atoms) and a-NMO (without Ru atoms), E_{Ru} is the total energy of the Ru metal atom in a-RNMO's most stable bulk structure. $U_{diss(metal, bulk)}$ denotes the standard dissolution potential of the bulk metal, and n represents the number of electrons transferred during the dissolution process. Based on the definition, $E_f < 0$ eV and $U_{diss} > 0$ V vs. SHE were considered thermodynamically and electrochemically stable, respectively.

OER pathways. In alkaline media, the OER proceeds via a four-electron transfer pathway, widely employed to quantify catalytic activity^{78,79}:



where * designates an active site on the catalytic surface, OOH^* , O^* , and OH^* denote the corresponding absorbed intermediates, respectively.

The Gibbs free energy change for the multistep OER can be expressed as follows⁸⁰:

$$\Delta G = \Delta E + \Delta E_{ZPE} - T\Delta S + k_B T \times \ln 10 \times pH \quad (11)$$

where ΔE represents the total energy difference between the reactants and products, obtained through DFT calculations. ΔE_{ZPE} corresponds to the vibrational frequencies of the adsorbed species. The specific values are provided in Supplementary Table 8. ΔS denotes the entropy change, with the temperature T at 298.15 K. $k_B T \times \ln 10 \times pH$ is the corrected value as a pH different from 0. The pH value is taken as 14 in this result. The overpotential of the OER is then determined as follows

$$\eta_{OER} = \frac{\Delta G_{\max}}{e} - 1.23 \quad (12)$$

Here, ΔG_{\max} refers to the maximum Gibbs free energy change among four reaction steps, given by Eqs. (6)–(10); 1.23 V is the thermodynamic equilibrium potential of water for $pH = 0$ at a temperature of $T = 298.15$ K. The atomic coordinates of the optimized computational models are given in Supplementary Data 1.

Data availability

All relevant data are available from the corresponding authors on request. Source data are provided in this paper. Source data are provided with this paper.

References

- Walter, M. G. et al. Solar water splitting cells. *Chem. Rev.* **110**, 6446–6473 (2010).
- Ding, H., Liu, H., Chu, W., Wu, C. & Xie, Y. Structural transformation of heterogeneous materials for electrocatalytic oxygen evolution reaction. *Chem. Rev.* **121**, 13174–13212 (2021).
- Hong, W. T. et al. Toward the rational design of non-precious transition metal oxides for oxygen electrocatalysis. *Energy Environ. Sci.* **8**, 1404–1427 (2015).
- Bloor, L. G., Molina, P. I., Symes, M. D. & Cronin, L. Low pH electrolytic water splitting using earth-abundant metastable catalysts that self-assemble in situ. *J. Am. Chem. Soc.* **136**, 3304–3311 (2014).
- Guo H-MY, D. an-D. an, Chi, J. un & Shao, Z. hi-G. ang Self-supporting NiFe LDHs@Co-OH-CO₃ nanorod array electrode for alkaline anion exchange membrane water electrolyzer. *J. Electrochem.* **28**, 2214003 (2022).
- Chen, F.-Y., Wu, Z.-Y., Adler, Z. & Wang, H. Stability challenges of electrocatalytic oxygen evolution reaction: From mechanistic understanding to reactor design. *Joule* **5**, 1704–1731 (2021).
- Shi, S. et al. High-entropy catalysts for electrochemical water-electrolysis of hydrogen evolution and oxygen evolution reactions. *Front. Energy* **18**, 265–290 (2024).
- Zhao, S. et al. Structural transformation of highly active metal–organic framework electrocatalysts during the oxygen evolution reaction. *Nat. Energy* **5**, 881–890 (2020).
- Sun, F. et al. Exploring structural evolution behaviors of ligand-defect-rich ferrocene-based metal-organic frameworks for electrochemical oxygen evolution via operando X-ray absorption spectroscopy. *Adv. Energy Mater.* **14**, 2400875 (2024).
- Zhu, J., Qian, J., Peng, X., Xia, B. & Gao, D. Etching-induced surface reconstruction of NiMoO₄ for oxygen evolution reaction. *Nano-Micro Lett.* **15**, 30 (2023).
- Wang, Y. et al. Anion etching for accessing rapid and deep self-reconstruction of precatalysts for water oxidation. *Matter* **3**, 2124–2137 (2020).
- Huang, H. et al. Unusual double ligand holes as catalytic active sites in LiNiO₂. *Nat. Commun.* **14**, 2112 (2023).
- Yao, Y. et al. Facet-dependent surface restructuring on nickel (oxy) hydroxides: a self-activation process for enhanced oxygen evolution reaction. *J. Am. Chem. Soc.* **146**, 15219–15229 (2024).
- Wu, Y. et al. Triggering lattice oxygen activation of single-atomic Mo sites anchored on Ni–Fe oxyhydroxides nanoarrays for electrochemical water oxidation. *Adv. Mater.* **34**, 2202523 (2022).
- Hu, Y. et al. Single Ru atoms stabilized by hybrid amorphous/crystalline FeCoNi layered double hydroxide for ultraefficient oxygen evolution. *Adv. Energy Mater.* **11**, 2002816 (2021).
- Goldsmith, B. R., Peters, B., Johnson, J. K., Gates, B. C. & Scott, S. L. Beyond ordered materials: understanding catalytic sites on amorphous solids. *ACS Catal.* **7**, 7543–7557 (2017).
- Liu, X. et al. Comprehensive understandings into complete reconstruction of precatalysts: synthesis, applications, and characterizations. *Adv. Mater.* **33**, 2007344 (2021).
- Wang, L., Wang, H. & Lu, J. Local chemical environment effect in single-atom catalysis. *Chem. Catal.* **3**, 100492 (2023).
- Zhu, Y., Wang, J. & Ma, J. Recent progress on non-carbon-supported single-atom catalysts for electrochemical conversion of green energy. *Small Sci.* **3**, 2300010 (2023).
- Wei, S. et al. Direct observation of noble metal nanoparticles transforming to thermally stable single atoms. *Nat. Nanotechnol.* **13**, 856–861 (2018).
- Shuiyun, S. H. E. N. LZ, Junliang ZHANG. promising approach for preparing metallic single-atom catalysts: electrochemical deposition. *Front. Energy* **16**, 537–541 (2022).
- Wang, L. et al. Manipulating the microenvironment of single atoms by switching support crystallinity for industrial hydrogen evolution. *Angew. Chem. Int. Ed.* **63**, e202317220 (2024).
- Liu, Y. et al. Unraveling the function of metal-amorphous support interactions in single-atom electrocatalytic hydrogen evolution. *Angew. Chem. Int. Ed.* **61**, e202114160 (2022).
- Cai, C. et al. Ultrahigh oxygen evolution reaction activity achieved using Ir single atoms on amorphous CoO_x nanosheets. *ACS Catal.* **11**, 123–130 (2021).
- Timoshenko, J. & Roldan Cuenya, B. In situ/operando electrocatalyst characterization by x-ray absorption spectroscopy. *Chem. Rev.* **121**, 882–961 (2021).
- Müller, O., Nachtegaal, M., Just, J., Lützenkirchen-Hecht, D. & Frahm, R. Quick-EXAFS setup at the SuperXAS beamline for in situ X-ray absorption spectroscopy with 10 ms time resolution. *J. Synchrotron Radiat.* **23**, 260–266 (2016).
- Zhang, B. et al. Homogeneously dispersed multimetal oxygen-evolving catalysts. *Science* **352**, 333–337 (2016).
- Billinge S. J. L. et al. 10.09 - Local structure determination using total scattering data. In: *Comprehensive Inorganic Chemistry III (Third Edition)* (eds Reedijk J, Poepelmeier KR). Elsevier (2023).

29. Egami T., Billinge S. J. L. *Underneath the Bragg Peaks: Structural Analysis of Complex Materials*. In: *Pergamon Materials Series* (eds Egami T., Billinge S. J. L.). 2nd edn. Pergamon materials series (2012).
30. Ye, C. et al. Activating metal oxides nanocatalysts for electrocatalytic water oxidation by quenching-induced near-surface metal atom functionality. *J. Am. Chem. Soc.* **143**, 14169–14177 (2021).
31. Zhang, J. et al. Interface engineering of MoS₂/Ni₃S₂ heterostructures for highly enhanced electrochemical overall-water-splitting activity. *Angew. Chem. Int. Ed.* **55**, 6702–6707 (2016).
32. Zhang, Z., Ma, X. & Tang, J. Porous NiMoO_{4-x}/MoO₂ hybrids as highly effective electrocatalysts for the water splitting reaction. *J. Mater. Chem. A* **6**, 12361–12369 (2018).
33. van Oversteeg, C. H. M., Doan, H. Q., de Groot, F. M. F. & Cuk, T. In situ X-ray absorption spectroscopy of transition metal based water oxidation catalysts. *Chem. Soc. Rev.* **46**, 102–125 (2017).
34. Guan, D. et al. Exceptionally robust face-sharing motifs enable efficient and durable water oxidation. *Adv. Mater.* **33**, 2103392 (2021).
35. Agrestini, S. et al. Nature of the magnetism of iridium in the double perovskite Sr₂ColrO₆. *Phys. Rev. B* **100**, 0144443 (2019).
36. Wong, J., Lytle, F. W., Messmer, R. P. & Maylotte, D. H. K-edge absorption spectra of selected vanadium compounds. *Phys. Rev. B* **30**, 5596–5610 (1984).
37. Joseph, D., Basu, S., Jha, S. N. & Bhattacharyya, D. Chemical shifts of K-X-ray absorption edges on copper in different compounds by X-ray absorption spectroscopy (XAS) with Synchrotron radiation. *Nucl. Instrum. Methods Phys. Res. B* **274**, 126–128 (2012).
38. Su, H. et al. In-situ spectroscopic observation of dynamic-coupling oxygen on atomically dispersed iridium electrocatalyst for acidic water oxidation. *Nat. Commun.* **12**, 6118 (2021).
39. Jiang, J. et al. Atomic-level insight into super-efficient electrocatalytic oxygen evolution on iron and vanadium co-doped nickel (oxy)hydroxide. *Nat. Commun.* **9**, 2885 (2018).
40. Kirshenbaum, K. et al. In situ visualization of Li/Ag₂VP₂O₈ batteries revealing rate-dependent discharge mechanism. *Science* **347**, 149–154 (2015).
41. Kongmark, C. et al. Synthesis of γ-Bi₂MoO₆ catalyst studied by combined high-resolution powder diffraction, XANES and Raman spectroscopy. *Catal. Today* **157**, 257–262 (2010).
42. Kuzmin A., Purans J. X-ray absorption spectroscopy study of the local environment around tungsten and molybdenum ions in tungsten-phosphate and molybdenum-phosphate glasses. In: *Proc. SPIE* (1997).
43. Rocca, F., Kuzmin, A., Mustarelli, P., Tomasi, C. & Magistris, A. XANES and EXAFS at Mo K-edge in (Agl)_{1-x}(Ag₂MoO₄)_x glasses and crystals. *Solid State Ion.* **121**, 189–192 (1999).
44. Lee, S., Chu, Y.-C., Bai, L., Chen, H. M. & Hu, X. Operando identification of a side-on nickel superoxide intermediate and the mechanism of oxygen evolution on nickel oxyhydroxide. *Chem. Catal.* **3**, 100475 (2023).
45. Cai, M. et al. Formation and stabilization of NiOOH by introducing α-FeOOH in LDH: composite electrocatalyst for oxygen evolution and urea oxidation reactions. *Adv. Mater.* **35**, 2209338 (2023).
46. Abdel-Dayem, H. M. Dynamic phenomena during reduction of α-NiMoO₄ in different atmospheres: in-situ thermo-raman spectroscopy study. *Ind. Eng. Chem. Res.* **46**, 2466–2472 (2007).
47. Ozkan, U. Schrader GL. NiMoO₄ selective oxidation catalysts containing excess MoO₃ for the conversion of C4 hydrocarbons to maleic anhydride: I. Preparation and characterization. *J. Catal.* **95**, 120–136 (1985).
48. Duan, Y. et al. Scaled-up synthesis of amorphous NiFeMo oxides and their rapid surface reconstruction for superior oxygen evolution catalysis. *Angew. Chem. Int. Ed.* **58**, 15772–15777 (2019).
49. Choi, J. et al. Interface engineered NiFe₂O_{4-x}/NiMoO₄ nanowire arrays for electrochemical oxygen evolution. *Appl. Catal. B: Environ.* **286**, 119857 (2021).
50. Zeng, K. et al. Molybdenum-leaching induced rapid surface reconstruction of amorphous/crystalline heterostructured trimetal oxides pre-catalyst for efficient water splitting and Zn-air batteries. *Energy Storage Mater.* **60**, 102806 (2023).
51. Rodriguez, J. A., Hanson, J. C., Chaturvedi, S., Maiti, A. & Brito, J. L. Phase transformations and electronic properties in mixed-metal oxides: Experimental and theoretical studies on the behavior of NiMoO₄ and MgMoO₄. *J. Chem. Phys.* **112**, 935–945 (2000).
52. Oudghiri-Hassani, H. & Al Wadaani, F. Preparation, characterization and catalytic activity of nickel molybdate (NiMoO₄) nanoparticles. *Molecules* **23**, 273 (2018).
53. Karmakar, S. & Behera, D. Band-correlated barrier-hopping conduction in α-NiMoO₄ micro-crystals and comparison of its energy storage performance with MWCNT-integrated complex. *J. Mater. Sci. Mater. Electron.* **31**, 5336–5352 (2020).
54. Huang, J. et al. Identification of key reversible intermediates in self-reconstructed nickel-based hybrid electrocatalysts for oxygen evolution. *Angew. Chem. Int. Ed.* **58**, 17458–17464 (2019).
55. Huang, Y., Wang, Z., Xiao, H., Liu, Q. & Wang, X. Activating and stabilizing lattice oxygen via self-adaptive Zn-NiOOH Sub-nanowires for oxygen evolution reaction. *J. Am. Chem. Soc.* **146**, 29006–29016 (2024).
56. Luo, X. et al. Fe-S dually modulated adsorbate evolution and lattice oxygen compatible mechanism for water oxidation. *Nat. Commun.* **15**, 8293 (2024).
57. Wei, J. et al. Sequential oxygen evolution and decoupled water splitting via electrochemical redox reaction of nickel hydroxides. *Nat. Commun.* **15**, 9012 (2024).
58. Guo, X. et al. Tackling the activity and selectivity challenges of electrocatalysts toward the nitrogen reduction reaction via atomically dispersed biatom catalysts. *J. Am. Chem. Soc.* **142**, 5709–5721 (2020).
59. Egami T., Billinge S. J. L. Preface. In: *Pergamon Materials Series* (eds Egami T., Billinge SJL). Pergamon (2003).
60. Billinge S. et al. Local structure determination using total scattering data. In: *Local Structure Determination Using Total Scattering Data* (2021).
61. Chupas, P. J. et al. Rapid-acquisition pair distribution function (RA-PDF) analysis. *J. Appl. Crystallogr.* **36**, 1342–1347 (2003).
62. Kieffer, J. & Karkoulis, D. PyFAI, a versatile library for azimuthal regrouping. *J. Phys.: Conf. Ser.* **425**, 202012 (2013).
63. Juhas, P., Davis, T., Farrow, C. L. & Billinge, S. J. L. PDFgetX3: a rapid and highly automatable program for processing powder diffraction data into total scattering pair distribution functions. *J. Appl. Crystallogr.* **46**, 560–566 (2013).
64. Farrow, C. L. et al. PDFfit2 and PDFgui: computer programs for studying nanostructure in crystals. *J. Phys. Condens. Matter* **19**, 335219 (2007).
65. Proffen, T. & Billinge, S. J. L. PDFFIT, a program for full profile structural refinement of the atomic pair distribution function. *J. Appl. Crystallogr.* **32**, 572–575 (1999).
66. Kresse, G. & Hafner, J. Ab initio molecular dynamics for liquid metals. *Phys. Rev. B* **47**, 558–561 (1993).
67. Kresse, G. & Furthmüller, J. Efficiency of ab-initio total energy calculations for metals and semiconductors using a plane-wave basis set. *Comput. Mater. Sci.* **6**, 15–50 (1996).
68. Blöchl, P. E. Projector augmented-wave method. *Phys. Rev. B* **50**, 17953–17979 (1994).
69. Kresse, G. & Joubert, D. From ultrasoft pseudopotentials to the projector augmented-wave method. *Phys. Rev. B* **59**, 1758–1775 (1999).

70. Perdew, J. P., Burke, K. & Ernzerhof, M. Generalized gradient approximation made simple. *Phys. Rev. Lett.* **77**, 3865–3868 (1996).
71. Kresse, G. & Furthmüller, J. Efficient iterative schemes for ab initio total-energy calculations using a plane-wave basis set. *Phys. Rev. B* **54**, 11169–11186 (1996).
72. Monkhorst, H. J. & Pack, J. D. Special points for Brillouin-zone integrations. *Phys. Rev. B* **13**, 5188–5192 (1976).
73. Li, X. et al. Phthalocyanine-supported single-atom catalysts as a promising bifunctional electrocatalyst for ORR/OER: A computational study. *ChemPhysMater* **1**, 237–245 (2022).
74. Grimme, S. Semiempirical GGA-type density functional constructed with a long-range dispersion correction. *J. Comput. Chem.* **27**, 1787–1799 (2006).
75. Mathew, K., Sundararaman, R., Letchworth-Weaver, K., Arias, T. A. & Hennig, R. G. Implicit solvation model for density-functional study of nanocrystal surfaces and reaction pathways. *J. Chem. Phys.* **140**, 084106 (2014).
76. Bader, R. F. W. A quantum theory of molecular structure and its applications. *Chem. Rev.* **91**, 893–928 (1991).
77. Henkelman, G., Arnaldsson, A. & Jónsson, H. A fast and robust algorithm for Bader decomposition of charge density. *Comput. Mater. Sci.* **36**, 354–360 (2006).
78. Nørskov, J. K. et al. Trends in the exchange current for hydrogen evolution. *J. Electrochem. Soc.* **152**, J23 (2005).
79. del Cueto, M., Ocón, P. & Poyato, J. M. L. Comparative study of oxygen reduction reaction mechanism on nitrogen-, phosphorus-, and boron-doped graphene surfaces for fuel cell applications. *J. Phys. Chem. C* **119**, 2004–2009 (2015).
80. Nørskov, J. K. et al. Origin of the overpotential for oxygen reduction at a fuel-cell cathode. *J. Phys. Chem. B* **108**, 17886–17892 (2004).

Acknowledgements

The work leading to these results has received funding from the Scientific Research Innovation Capability Support Project for Young Faculty (ZYGXQNJSKYCXNLZCXM-E10), the National Natural Science Foundation of China (22179098) and Xiaomi Young Talents Program to J.M. L.Y. acknowledges support from the National Natural Science Foundation of China (52302193). X.Y. acknowledges support from the National Natural Science Foundation of China (52302302). W.-H.H. acknowledges the support from the National Science and Technology Council (NSTC) in Taiwan (NSTC 113-2628-E-011-004-MY3) and National Taiwan University of Science and Technology & Bandung Institute of Technology Joint Research Program (ITB-NTUST-2024-01). The synchrotron radiation PDF experiments were performed at BLO8W of SPring-8 with the approval of Japan Synchrotron Radiation Research Institute (JASRI, Proposal No. 2023A1347).

Author contributions

J.M. conceived and coordinated the project. J.L., Y.Z. and J.M. designed the experiments. J.L., Y.Z., C.L. and L.Y. conducted the experimental measurements. J.L., Y.Z., Q.Z., S.G., W.-H.H., M.-H.Y. and H.C. performed the experimental optimization, data analysis, and discussions. J.R. and X.Y. conducted the theoretical calculations. J.L., N.A.-V., H.C. and J.M. wrote the paper with the contributions of all co-authors.

Competing interests

The authors declare no competing interests.

Additional information

Supplementary information The online version contains supplementary material available at <https://doi.org/10.1038/s41467-025-63870-9>.

Correspondence and requests for materials should be addressed to Wei-Hsiang Huang, Xiaohua Yu, Hongfei Cheng or Jiwei Ma.

Peer review information *Nature Communications* thanks Jinghua Guo, Jing-Li Luo and the other anonymous reviewer(s) for their contribution to the peer review of this work. A peer review file is available.

Reprints and permissions information is available at <http://www.nature.com/reprints>

Publisher's note Springer Nature remains neutral with regard to jurisdictional claims in published maps and institutional affiliations.

Open Access This article is licensed under a Creative Commons Attribution-NonCommercial-NoDerivatives 4.0 International License, which permits any non-commercial use, sharing, distribution and reproduction in any medium or format, as long as you give appropriate credit to the original author(s) and the source, provide a link to the Creative Commons licence, and indicate if you modified the licensed material. You do not have permission under this licence to share adapted material derived from this article or parts of it. The images or other third party material in this article are included in the article's Creative Commons licence, unless indicated otherwise in a credit line to the material. If material is not included in the article's Creative Commons licence and your intended use is not permitted by statutory regulation or exceeds the permitted use, you will need to obtain permission directly from the copyright holder. To view a copy of this licence, visit <http://creativecommons.org/licenses/by-nc-nd/4.0/>.

© The Author(s) 2025